nature materials

LETTERS

PUBLISHED ONLINE: 4 DECEMBER 2017 | DOI: 10.1038/NMAT5038

Sub-nanometre channels embedded in two-dimensional materials

Yimo Han[1†], Ming-Yang Li[2,3†], Gang-Seob Jung[4†], Mark A. Marsalis[5], Zhao Qin[4], Markus J. Buehler[4], Lain-Jong Li[2*] and David A. Muller[1,6*]

Two-dimensional (2D) materials are among the most promising candidates for next-generation electronics due to their atomic thinness, allowing for flexible transparent electronics and ultimate length scaling[1]. Thus far, atomically thin p–n junctions[2–8], metal–semiconductor contacts[9–11], and metal–insulator barriers[12–14] have been demonstrated. Although 2D materials achieve the thinnest possible devices, precise nanoscale control over the lateral dimensions is also necessary. Here, we report the direct synthesis of sub-nanometre-wide one-dimensional (1D) MoS_2 channels embedded within WSe_2 monolayers, using a dislocation-catalysed approach. The 1D channels have edges free of misfit dislocations and dangling bonds, forming a coherent interface with the embedding 2D matrix. Periodic dislocation arrays produce 2D superlattices of coherent MoS_2 1D channels in WSe_2. Using molecular dynamics simulations, we have identified other combinations of 2D materials where 1D channels can also be formed. The electronic band structure of these 1D channels offers the promise of carrier confinement in a direct-gap material and the charge separation needed to access the ultimate length scales necessary for future electronic applications.

Reducing the lateral scale of atomically thin 2D devices is crucial not only to realize competitive electronic device applications, but also for reaching the length scales needed for quantum confinement. Thus far, the many 2D heterostructure devices rely on lithographic patterning of one 2D layer followed by the growth of another in the patterned areas[9–12]. Although this technique provides spatial control down to below a hundred nanometres or so, the nature of the lithographic patterning creates atomic defects and contamination. Consequently, the atomic junctions in these heterostructures contain electronic defect states, impacting device performance. Recently, the growth of micrometre-sized in-plane epitaxial interfaces between 2D materials has been reported using chemical vapour deposition (CVD) methods[3–8,13,14]. Theory predicts a tunable carrier confinement[15] and the formation of a 1D electron gas[16] at the abrupt and coherent interfaces in heterostructures of 2D materials that are just a few atoms wide. The atomic-scale heterostructures are usually chosen for computational convenience, but there would be benefits in realizing such narrow physical structures. For example, in contrast to broad in-plane heterostructures, which ultimately generate misfit dislocations to release the lattice strain, thin channels can sustain large strains without relaxation, and hence access a wider range of electronic band structures. Just as in bulk materials, dislocation formation can be suppressed below a critical film width[17], which scales inversely with the desired strain—several nanometres are typical for mismatch in the family of 2D transition metal dichalcogenides (TMDs). The thin channels always have one dimension below their critical thickness, ensuring stability against dislocation formation at the strained epitaxial interfaces. Eliminating interfacial dislocations, whose cores are 4|8 or 5|7 member ring structures, is key, as these are generally expected to introduce undesirable mid-gap states[15,18,19].

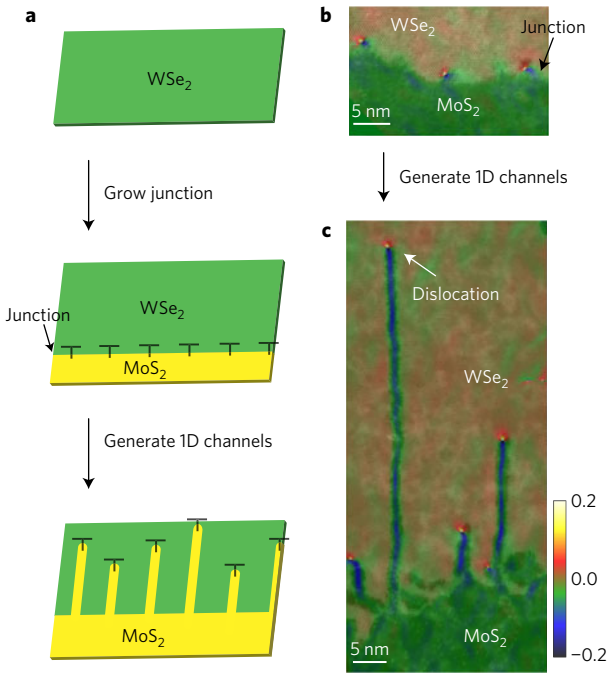

Figure 1 | Formation of 1D channels. a, Schematic of the patterning process guided by misfit dislocations (marked as 'T') at the MoS_2–WSe_2 lateral heterojunction. **b**,**c**, Atomic-resolution ADF-STEM images overlaid with their ε_{xx} strain maps (see Fig. 2 for more details) identifying the periodic dislocations at the interface of MoS_2 and WSe_2 (**b**) and the 1D channels created by chemically driven migration of the interfacial dislocations as additional S and Mo atoms are added (**c**). Strain maps refer to the WSe_2 lattice.

[1]School of Applied and Engineering Physics, Cornell University, Ithaca, New York 14850, USA. [2]Physical Science and Engineering Division, King Abdullah University of Science and Technology, Thuwal 23955-6900, Kingdom of Saudi Arabia. [3]Research Center for Applied Sciences, Academia Sinica, Taipei 10617, Taiwan. [4]Department of Civil and Environmental Engineering, MIT, Cambridge, Massachusetts 02139, USA. [5]Department of Physics, Texas Tech University, Lubbock, Texas 79416, USA. [6]Kavli Institute at Cornell for Nanoscale Science, Cornell University, Ithaca, New York 14850, USA. [†]These authors contributed equally to this work. *e-mail: lance.li@kaust.edu.sa; david.a.muller@cornell.edu

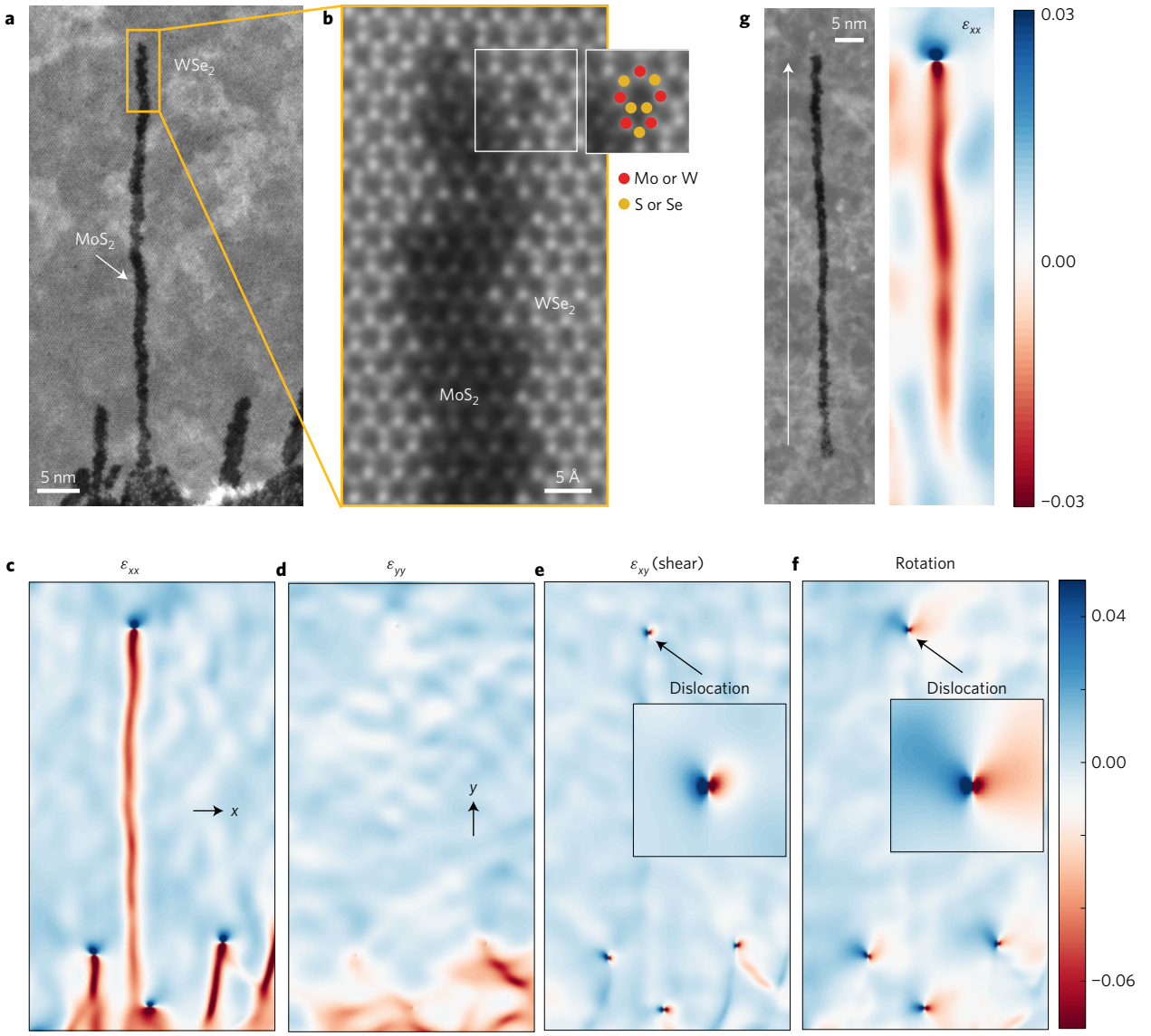

Figure 2 | Strain maps of the 1D channels. a,**b**, ADF-STEM image of MoS_2 1D channels embedded within WSe_2. The channel ends with the 5|7 dislocation (white box in **b**). The same section is shown to the right with the atoms labelled. **c**,**d**, Geometric phase analysis (GPA) of the 1D MoS_2 in **a** with uniaxial strain components ε_{xx} (**c**) and ε_{yy} (**d**). All the strain is in reference to the WSe_2 lattice. The ε_{xx} clearly distinguishes the two lattices mainly due to the lattice mismatch, while the ε_{yy} indicates a high uniaxial tensile strain in the 1D MoS_2 which is lattice mismatched with respect to the WSe_2. **e**,**f**, Shear strain and rotation map (in radians), respectively, indicating the position and orientation of the dislocations. **g**, ADF-STEM image (left) and its ε_{xx} strain map (right) of a MoS_2 1D channel formed from an intrinsic 5|7 dislocation in WSe_2, which matches the results found in channels arising from the heterojunction interface.

Here, we report an approach for fabricating coherent 1D channels within 2D heterostructures (Fig. 1). These channels possess sub-nanometre widths and atomically coherent sidewalls free of misfit dislocations and dangling bonds. We start with a lateral interface between two 2D TMDs, MoS_2 and WSe_2, whose lattice mismatch provides an array of interfacial misfit dislocations (Fig. 1b and Supplementary Fig. 1). We introduce growth precursors that provide a high chemical potential for the channel material. The higher reactivity in the core of the misfit dislocations allows the channel atoms (Mo and S) to be inserted into the dislocation core, thus pushing the dislocations away from the original interface, forming 1D MoS_2 channels in a trail behind the advancing core (Fig. 1c and Supplementary Fig. 2). The dislocation-catalysed growth is essentially the flat analogue of the semiconductor nanowires whose growth from seeded catalysts has played an important role in semiconductor nanoscience. (See Methods for details on sample preparation and synthesis.)

Atomic-resolution annular dark-field scanning transmission electron microscopy (ADF-STEM) imaging shows that the epitaxial interface between the body of the channel and the host matrix is coherently connected (Fig. 2a,b). Meanwhile, a pentagon–heptagon (5|7) dislocation (heptagon pointing up) is found at the terminus of all 1D channels (Fig. 2b). The difference in the atomic number between Mo and W provides high contrast between the WSe_2 template and the newly grown MoS_2 channels in the ADF-STEM images. Supplementary Fig. 3 shows colour-coded ADF-STEM images that make the lighter Mo and S atoms more visible. (See Methods for ADF-STEM details.)

The as-grown heterostructures of the TMDs must contain strain, due to the bond mismatch to create an epitaxial interface. Applying a geometric phase analysis (GPA)[20] to the ADF-STEM image in Fig. 2a, we are able to elucidate the strain distribution in and around this 1D channel in its 2D matrix, as plotted in Fig. 2c–f (see Supplementary Fig. 4 and Methods for more details). For

GPA, the WSe_2 lattice parameter was chosen as the reference or zero strain (−0.036 would correspond to relaxed MoS_2 sheets, consistent with the 3.6% lattice difference measured from the electron diffraction of the MoS_2 and WSe_2 layers in Supplementary Fig. 1a). Along the x-axis, there is significant difference in the strain map between the 2D WSe_2 and 1D MoS_2 channels, arising mainly from the lattice mismatch (Fig. 2c). In contrast, the y-axis strain map reveals that MoS_2 channels have an identical lattice spacing to that of the host WSe_2 (Fig. 2d), indicating a high uniaxial tensile strain along the y direction (See Supplementary Fig. 5 for detailed strain analysis on a single channel). Therefore, the newly synthesized 1D channel maintains coherency with the WSe_2 matrix, and is strain accommodated, which effectively avoids the generation of misfit dislocations along the channel. The shear map and rotation map (Fig. 2e,f) display the position and orientation of the dislocations as dipole fields, confirming all dislocations have the same orientation and migrate upwards (that is, away from the original hetero-interface).

Growth of the 1D channels is not limited to the interfacial misfit dislocations at the heterostructure interface of the two 2D materials. They can also be generated from intrinsic 5|7 dislocations implanted within the WSe_2 film. The ADF-STEM image and corresponding ε_{xx} strain map (Fig. 2g) of a MoS_2 1D channel show that it was formed from an intrinsic catalyst dislocation migrating in the direction of the heptagon (additional information provided in Supplementary Fig. 6). The isolated 1D channel is 70 nm in length and 1.5 nm in width, surrounded by monolayer WSe_2 on all sides, showing a high aspect ratio of about 47:1 (length to width).

To understand the catalytic role of 5|7 dislocations, we utilized a reactive force field with newly developed parameters based on density function theory (DFT) calculations and an accelerated molecular dynamics (MD) simulation (details in Supplementary Discussions 1–3). Our method captures the dynamics of the chemical bonds breaking and reforming, which is difficult to model using conventional non-reactive MD simulations. We found that, unlike other hexagonal rings, the dislocation core allows the precursor atoms to be inserted, which acts as the driving force for the dislocation-catalysed growth. The precursors first open the catalyst 5|7 dislocation, which admits the Mo insertion (Fig. 3a). This step makes S atoms insufficient to finish the dislocation migration, leaving unsaturated dangling bonds in the system, and hence the lattice around the dislocation core reconstructs to find more energetically favourable structures. Afterwards, as more S atoms are absorbed from the environment, the lattice relaxes and forms the next dislocation (Fig. 3b). While repeating these two key steps, the previously occupied W and Se atoms near the dislocation core have a certain probability to leave the 2D sheet, and those sites are replaced by the Mo and S precursors during the reconstruction and relaxation. Altogether, the entire process eventually leaves a narrow MoS_2 trail behind it (see Supplementary Discussion 4 and Supplementary Movies 1–8 for more details). The circles in Fig. 3c indicate the additional Mo and S atoms placed at the dislocation during each migration step of the catalyst. The additional Mo and S atoms contribute to a 1.4% compressive strain in the x direction within the channels (Supplementary Fig. 5c).

Due to the crystal geometry of the hexagonal lattice, the migration of the dislocation has two choices: 30° to the right or left (blue or red arrows in Fig. 3c), where the reference lattice orientation is shown as the grey hexagons. MD simulation shows the lateral strain field provides a local restoring force that guides dislocations back towards a straight line along the interface normal, as shown in Supplementary Fig. 7. Thus, the dislocation zigzags about a straight line perpendicular to the macroscopic interface, and is ultimately oriented in the heptagon direction, as shown in Fig. 3d.

The dislocation movement out of its slip plane (climb[21]) also occurs in a 3D epitaxial interface, due to the diffusion of vacancies

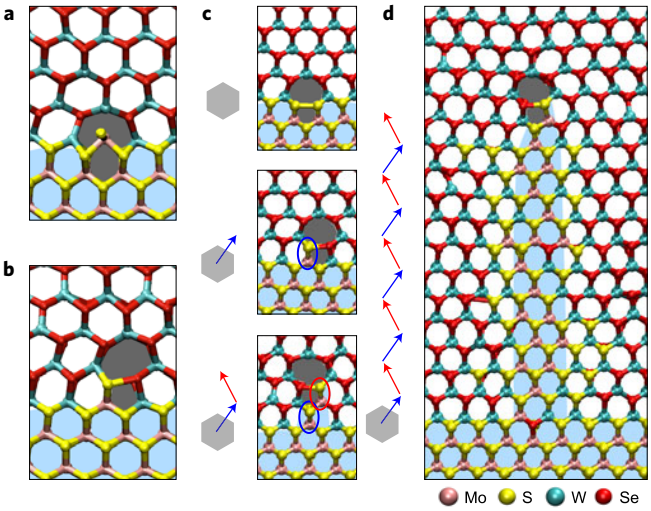

Figure 3 | Molecular dynamics (MD) simulation of the 1D channel formation. a,**b**, MD simulation of the process of Mo inserting into the pentagon ring of a 5|7 dislocation (**a**) and the formation of the next 5|7 dislocation (**b**). **c**, MD simulation of each step for the patterning process. The 5|7 dislocation can migrate 30° to the right (blue arrow) or 30° to the left (red arrow). **d**, The iteration of adding excess Mo and S atoms forms the 1D MoS_2 channel in WSe_2, unveiling the chemically driven mechanism for the formation of the 1D channels.

or interstitial atoms. In the bulk, this typically does not produce any major effects. In contrast, misfit dislocations in 2D materials can directly take (release) atoms from (to) the environment, suggesting persistent climbs that can be used to pattern 1D channels by controlling the precursors and growth time. Statistically, 76% of dislocations tend to migrate and form 1D channels under our optimized growth conditions. Dislocations that did not move tended to have complicated local interface geometries (Supplementary Fig. 1). After measuring 150 1D channels, we achieved an averaged distance between neighbouring 1D channels of 10.9 (±0.9) nm, indicating a density of 92 (±8) 1D channels per micrometre along the interface between MoS_2 and WSe_2 (Supplementary Fig. 8a). A histogram of channel length is shown in Supplementary Fig. 8b, of which the longest channels reached 80 nm. The length of the 1D channels was strongly correlated with the width of the MoS_2 layer around the WSe_2 triangles, which is mainly determined by the precursor ratio (S:Mo) and the growth time (Supplementary Fig. 9), suggesting these are two key underlying control parameters. However, there is a limit to how long the MoS_2 channels can be grown. As the surrounding MoS_2 layer continues to grow, the channel growth ultimately becomes unstable—the 1D channels have the possibility to branch repeatedly and recursively, leading to tree-like structures that eventually consume the host material (Supplementary Figs 10 and 11).

Despite a variety of lengths, more than 90% of the 1D channels have widths that are less than 2 nm, confirming the high accuracy of the dislocation-guided patterning process (Supplementary Fig. 8c). For these ultra-narrow MoS_2 channels in WSe_2, DFT calculations (Supplementary Discussion 5) show a type II band alignment useful for highly localized carrier confinement and charge separation (Supplementary Fig. 12). Moreover, the strained 1D MoS_2 shows a direct bandgap, distinct from the indirect bandgap found in uniaxially strained 2D MoS_2 thin films[22]. In addition, the 1D channel sidewalls should be free of undesirable mid-gap states that occur due to dislocations and dangling bonds. Both are desirable properties for ultra-small monolayer electronic and optoelectronic applications.

The nature of the 1D growth can be used to create lateral 1D superlattices in 2D materials starting from a periodic dislocation

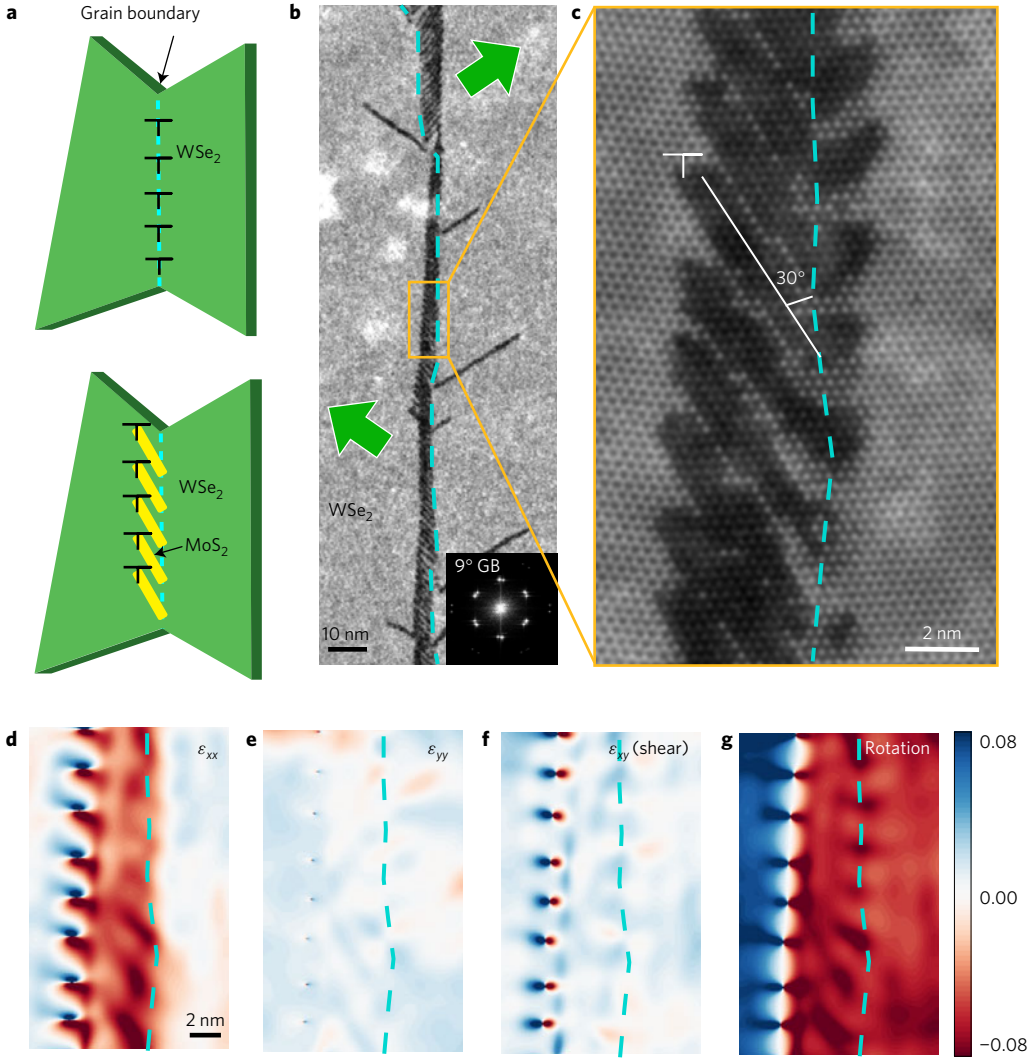

Figure 4 | Generation of a superlattice at a grain boundary. a, Schematic of the superlattice formation where the top (bottom) panel depicts the grain boundary before (after) the patterning process. **b**, ADF-STEM image of a superlattice grown from the periodic dislocations at the WSe_2 grain boundary with 9° rotation (2 nm spacing between dislocations). All blue dashed lines indicate the position of the original curved grain boundary. The dislocations migrate in different directions (indicated by the green arrows), thus forming a shifted but straight grain boundary. **c**, Magnified ADF-STEM image with one of the identical dislocations marked by a 'T'. **d**–**g**, GPA of the image in **c**, showing that dislocations preserve their periodicity and orientations during the migration.

chain, as illustrated in Fig. 4a. The most common structures with periodic dislocations are the grain boundaries of 2D materials[18,19,23,24]. At a typical low-angle WSe_2 grain boundary, where two grains with small rotation angles connect laterally to form a classic low-angle tilt boundary, the periodic arrays of 5|7 dislocation cores line up with a spacing $\sim b/\theta$. Here, b is the Burger's vector and θ is the tilt angle between the two grains, suggesting the grain boundary tilt angle can be used to control the 1D channel spacing. In theory, the dislocations are most stable when they lie vertically above one another with equal spacing[21]. To attain the lowest energy over large scales, the dislocations at the originally curved grain boundary (blue dashed line in Fig. 4b) migrate with an angle of 30° to the left (or to the right) of the heptagon direction (as indicated in Fig. 3c) to form a straight grain boundary. This is also observed in the GPA in Supplementary Fig. 13.

The magnified ADF-STEM image (Fig. 4c) shows a region where all catalyst dislocations migrate 30° to the left, forming ~1 nm nanowire arrays with sub-nanometre spacing. Figure 4d–g presents the strain maps of Fig. 4c, indicating that dislocations keep their periodicity and orientations after the translation, and the right-side lattice orientation is inherited. We note that in Fig. 4c, short branches appear also on the right side of the original grain boundary, but they have no dislocations at the ends. This can be understood as arising from individual dislocations wandering before they are propelled towards the left by other dislocations, suggesting a strong collective interaction between dislocations that can be used to control the patterning of 1D superlattices. This 1D superlattice formation is commonly observed at low-angle tilt grain boundaries lower than 10° (Supplementary Fig. 14 shows another example).

Our strategy to produce dislocation-free 1D channels suggests a general set of search criteria for other 2D materials. First, candidate materials need a source of dislocations, such as a low-angle grain boundary or lattice mismatched hetero-interface. Second, although the dislocations allow for an easier insertion and exchange of atoms, the substitutions need to be energetically favourable (for example, S for Se). We used MD simulations to identify other two-candidate systems for 1D-channel formation: 1D WS_2 in WSe_2 (a different 1D-channel material) and 1D MoS_2 in $MoSe_2$ (a different matrix material), both of which are lattice mismatched (see Supplementary Fig. 15 for simulation details). However, combinations of materials that have little lattice mismatch, such as MoS_2 and WS_2, will not form 1D channels due to the

lack of an initial source of catalyst dislocations (see Supplementary Fig. 16 for an experimental example). The lattice mismatch and displacement criteria allow us to predict candidate systems for 1D channel formation, and also provides a way to engineer the strain in the 1D channels by changing the 2D hosts.

Methods

Methods, including statements of data availability and any associated accession codes and references, are available in the online version of this paper.

Received 29 March 2017; accepted 23 October 2017; published online 4 December 2017

References

1. Franklin, A. D. Nanomaterials in transistors: from high-performance to thin-film applications. *Science* **349,** aab2550 (2015).
2. Lee, C.-H. *et al*. Atomically thin p–n junctions with van der Waals heterointerfaces. *Nat. Nanotech.* **9,** 676–681 (2014).
3. Gong, Y. *et al*. Vertical and in-plane heterostructures from WS_2/MoS_2 monolayers. *Nat. Mater.* **13,** 1135–1142 (2014).
4. Duan, X. *et al*. Lateral epitaxial growth of two-dimensional layered semiconductor heterojunctions. *Nat. Nanotech.* **9,** 1024–1030 (2014).
5. Huang, C. *et al*. Lateral heterojunctions within monolayer $MoSe_2$–WSe_2 semiconductors. *Nat. Mater.* **13,** 1096–1101 (2014).
6. Li, M. *et al*. Epitaxial growth of a monolayer WSe_2-MoS_2 lateral p–n junction with an atomically sharp interfaces. *Science* **349,** 524–528 (2015).
7. Gong, Y. *et al*. Two-step growth of two-dimensional WSe_2/$MoSe_2$ heterostructures. *Nano Lett.* **15,** 6135–6141 (2015).
8. Zhang, Z. *et al*. Robust epitaxial growth of two-dimensional heterostructures, multiheterostructures, and superlattices. *Science* http://dx.doi.org/10.1126/science.aan6814 (2017).
9. Ling, X. *et al*. Parallel stitching of 2D materials. *Adv. Mat.* **28,** 2322–2329 (2016).
10. Zhao, M. *et al*. Large-scale chemical assembly of atomically thin transistors and circuits. *Nat. Nanotech.* **11,** 954–959 (2016).
11. Guimaraes, M. H. D. *et al*. Atomically thin Ohmic edge contacts between two-dimensional materials. *ACS Nano* **10,** 6392–6399 (2016).
12. Levendorf, M. P. *et al*. Graphene and boron nitride lateral heterostructures for atomically thin circuitry. *Nature* **488,** 627–632 (2012).
13. Liu, L. *et al*. Heteroepitaxial growth of two-dimensional hexagonal boron nitride templated by graphene edges. *Science* **343,** 163–167 (2014).
14. Chen, L. *et al*. Oriented graphene nanoribbons embedded in hexagonal boron nitride trenches. *Nat. Commun.* **8,** 14703 (2017).
15. Kang, J. *et al*. Tuning carrier confinement in the MoS_2/WS_2 lateral heterostructure. *J. Phys. Chem. C* **119,** 9580–9586 (2015).
16. Rubel, O. One-dimensional electron gas in strained lateral heterostructures of single layer materials. *Sci. Rep.* **7,** 4316 (2017).
17. People, R. & Bean, J. Calculation of critical layer thickness versus lattice mismatch for Ge_xSi_{1-x}/Si strained-layer heterostructures. *Appl. Phys. Lett.* **47,** 322–324 (1985).
18. Van der Zande, A. M. *et al*. Grains and grain boundaries in highly crystalline monolayer molybdenum disulphide. *Nat. Mater.* **12,** 554–561 (2013).
19. Zou, X., Liu, Y. & Yakobson, B. I. Predicting dislocations and grain boundaries in two-dimensional metal-disulfides from the first principles. *Nano Lett.* **13,** 253–258 (2013).
20. Hytch, M. J., Snoeck, E. & Kilaas, R. Quantitative measurement of displacement and strain fields from HREM micrographs. *Ultramicroscopy* **74,** 131–146 (1998).
21. Hull, D. & Bacon, D. J. *Introduction to Dislocations* (Elsevier, 2011).
22. He, K. Experimental demonstration of continuous electronic structure tuning via strain in atomically thin MoS_2. *Nano Lett.* **13,** 2931–2936 (2013).
23. Huang, P. Y. *et al*. Grains and grain boundaries in single-layer graphene atomic patchwork quilts. *Nature* **469,** 389–392 (2011).
24. Huang, Y. L. *et al*. Bandgap tunability at single-layer molybdenum disulphide grain boundaries. *Nat. Commun.* **6,** 6298 (2015).

Acknowledgements

The authors acknowledge discussions with M. Zhao, L. Wang, C. Zhen, M. Holtz, H.-S. Kim, C. Gong, T. Cao, M. S. Ramos, L. F. Kourkoutis, B. Savitzky, M. Zhao, C.-J. Kim, K. Kang, J. Park, D. Jena and J. Sethna. This work made use of the electron microscopy facility of the Cornell Center for Materials Research (CCMR) with support from the National Science Foundation (NSF) Materials Research Science and Engineering Centers (MRSEC) program (DMR-1120296) and NSF Major Research Instrumentation Program (DMR-1429155). Y.H. and D.M. were supported by NSF Grant (DMR-1719875) and DOD-MURI (Grant No. FA9550-16-1-0031). G.-S.J., Z.Q. and M.J.B. acknowledge support by the Office of Naval Research (Grant No. N00014-16-1-233) and DOD-MURI (Grant No. FA9550-15-1-0514). We acknowledge support for supercomputing resources from the Supercomputing Center/KISTI (KSC-2017-C2-0013). M.-Y.L. and L.L. thank the support from King Abdullah University of Science and Technology (KAUST) and Academia Sinica.

Author contributions

Y.H., M.-Y.L. and G.-S.J. contributed equally to this work. Y.H. conceived the project. Electron microscopy and data analysis were carried out by Y.H., under the supervision of D.A.M., with help from M.A.M. Sample growth was done by M.-Y.L., under the supervision of L.L. The molecular dynamics simulations and density function theory calculations were conducted by G.-S.J. and Z.Q., under the supervision of M.J.B.

Additional information

Supplementary information is available in the online version of the paper. Reprints and permissions information is available online at www.nature.com/reprints. Publisher's note: Springer Nature remains neutral with regard to jurisdictional claims in published maps and institutional affiliations. Correspondence and requests for materials should be addressed to L.-J.L. or D.A.M.

Competing financial interests

The authors declare no competing financial interests.

Methods

Sample growth. First, the WSe_2 monolayers were grown on sapphire substrates using the chemical vapour deposition (CVD) method, with WO_3 and Se powders as the precursors carried by Ar (90 sccm) and H_2 (6 sccm) gases. The furnace was heated to 925 °C at a pressure of 15 torr for 15 min to grow WSe_2 monolayers, which contain sharp edges and grain boundaries. After cooling, the sample was placed in another furnace for the second step growth of MoS_2 monolayers, forming abrupt epitaxial junctions with misfit dislocations. During the second step, MoO_3 (at 760 °C) and S (at 190 °C) powders were used as the precursors carried by Ar gas flowing at 70 sccm at a pressure of 40 torr and a temperature of 760 °C for 10 min. However, in the second step, since the dislocations along the abrupt junctions and grain boundaries had already been exposed to the Mo and S precursors at such a high temperature, the patterning process had already begun and the 1D MoS_2 had been formed.

Transfer to TEM grids. The sample was coated with polymethyl methacrylate (PMMA) A4 resist to support the film during the transfer process. To detach the film from the sapphire substrate, the sample was placed in HF solution (HF:H_2O 1:3) for 15 min. After rinsing with deionized water several times, the sample was blow-dried and dipped into water—using the surface tension—to release the film from the substrate. With the film floating on the surface of the water, we applied a QUANTIFOIL holey carbon TEM grid to scoop the film. Afterwards, the TEM grid with samples was baked in vacuum (1×10^{-7} torr) at 350 °C for 5 h to remove the PMMA. Baking in vacuum is essential because the dislocations will degrade and form holes if baked in air.

ADF-STEM. ADF-STEM imaging was conducted using an aberration-corrected FEI TITAN operated at 120 kV with an approximately 15 pA probe current. The acquisition time per pixel was less than 8 ms, but multiple images (10–20) were acquired and cross-correlated afterwards to improve the signal to noise ratio and reduce the scan noise introduced by the sample drift. Despite the electron beam energy being above the knock-on damage threshold for WSe_2 and MoS_2, the low dose per image, in fact, avoided significant damage from ionization. A 30 mrad convergence angle and an approximately 40 mrad inner collection angle were used for all ADF-STEM images, whose contrast is proportional to Z^{γ}, where Z is the atomic number and $1.3 < \gamma < 2$. Therefore, the W, Se, Mo and S atoms can be distinguished easily by this Z-contrast imaging technique.

Geometric phase analysis. Geometric phase analysis (GPA) is a method for measuring and mapping strain fields from high-resolution electron microscope images[25]. It describes how the spatial frequency components (lattice fringes) of the image vary across the image field of view. Here in this work we applied GPA to atomic-resolution ADF-STEM images of MoS_2 1D channels embedded within WSe_2 monolayers. We used the GPA plugin[26] developed for Digital Micrograph, and the detailed process is described below and in Supplementary Fig. 4.

We first Fourier transform the atomic-resolution images (Supplementary Fig. 4a) to the power spectrum (Supplementary Fig. 4b). In the power spectrum, the strong Bragg-reflections are related to the unit cell of the crystalline structure of the material. A perfect crystal lattice gives rise to sharply peaked frequency components, while the broadening of the Bragg spots is due to the local lattice distortion in the material.

Instead of using a mask covering the entire first Brillouin zone, in practice, we placed circular Gaussian masks on two non-collinear reciprocal lattice vectors g_1 and g_2, as shown in Supplementary Fig. 4b in red and blue circles on the power spectrum. The size of the masks is smaller than the Brillouin zone. The resolution and smoothing set-up in Supplementary Fig. 4k defines the size and smoothing of the masks, which help to reduce noise and smooth the resulting images.

To calculate the phase image we convolved each region around reciprocal vector g_1 and g_2 with the masks. Afterwards, we performed an inversed Fourier transform to create a complex image that the phase image was calculated from.

$$P_g(\mathbf{r}) = \mathrm{Phase}[H_g'(\mathbf{r})] - 2\pi\mathbf{g}\cdot\mathbf{r} \quad (1)$$

where $H_g'(\mathbf{r})$ is the complex image from the inversed Fourier transform, and $\mathbf{g}$ is the reciprocal lattice vector where the mask was placed. The phase images corresponding to reciprocal lattice vector $\mathbf{g}_1$ and $\mathbf{g}_2$ are plotted in Supplementary Figs 4c and 4d after a renormalization between $\pm\pi$.

To determine the displacement field $\mathbf{u}$ we note that in its presence, the maximum of the fringes $\mathbf{r}$ is displaced by $\mathbf{u}$, and becomes $\mathbf{r}-\mathbf{u}$. In this case, we can write the intensity of Bragg filtered images that were produced by the Gaussian mask at $\mathbf{g}$:

$$B_g(\mathbf{r}) = 2A_g \cos[2\pi\mathbf{g}\cdot\mathbf{r} - 2\pi\mathbf{g}\cdot\mathbf{u} + P_g] \quad (2)$$

where the A_g is the amplitude, and P_g is an arbitrary constant phase that can be ignored. From equation (2), we note that the middle term is a phase term that depends on the lattice displacement field $\mathbf{u}$: $P_g(\mathbf{r}) = -2\pi\mathbf{g}\cdot\mathbf{u}$, which can be calculated by taking the inverse of $\mathbf{g}$:

$$\mathbf{u}(\mathbf{r}) = -\frac{1}{2\pi}[P_{g1}(\mathbf{r})\mathbf{a}_1 + P_{g2}(\mathbf{r})\mathbf{a}_2] \quad (3)$$

where $\mathbf{a}_1$ and $\mathbf{a}_2$ are the inverse of $\mathbf{g}_1$ and $\mathbf{g}_2$.

To determine the strain and rotation fields we first calculate the local distortion of the lattice from the gradient of the displacement field, defined as a 2×2 matrix:

$$e = \begin{pmatrix} e_{xx} & e_{xy} \\ e_{yx} & e_{yy} \end{pmatrix} = \begin{pmatrix} \frac{\partial u_x}{\partial x} & \frac{\partial u_x}{\partial y} \\ \frac{\partial u_y}{\partial x} & \frac{\partial u_y}{\partial y} \end{pmatrix} \quad (4)$$

The strain is given by the symmetric term $\varepsilon = (1/2)[e + e^{\mathrm{T}}]$ and the rigid rotation is described by the anti-symmetric term $\omega = (1/2)[e - e^{\mathrm{T}}]$. In this paper, the uniaxial strain can be calculated using $\varepsilon_{xx} = e_{xx}$, and $\varepsilon_{yy} = e_{yy}$, as shown in Supplementary Figs 4g and 4h, respectively. The shear strain field map shown in Supplementary Fig. 4i is calculated using $\varepsilon_{xy} = (e_{xy} + e_{yx})/2$. The rotation map displayed in Supplementary Fig. 4j is calculated by $\varepsilon_{\mathrm{rot}} = (e_{xy} - e_{yx})/2$.

In Supplementary Fig. 4k, we cropped the GPA plugin[2] control panel. In this software, 'a^*' displays the length of reciprocal lattice vector $\mathbf{g}_1$ in units of 1 nm^{-1} and 'b^*' shows that of $\mathbf{g}_2$. The local $|\mathbf{g}_1|$ and $|\mathbf{g}_2|$ are mapped in Supplementary Fig. 4e,f. Gamma represents the angle between $\mathbf{g}_1$ and $\mathbf{g}_2$ in degrees, while theta displays the angle between $\mathbf{g}_2$ and the horizontal axis (white arrow in Supplementary Fig. 4b). The resolution set-up defines the size of the Gaussian masks and the smoothing defines the mask edge smoothing. The 'refine G-vectors' button calculates the $\mathbf{g}$ vectors in the reference lattice region we selected, thus refining the centre of the masks. Here in this work we select the flat WSe_2 region as the reference lattice.

MD for the growth of a 1D MoS_2 channel. MD simulations in this study were performed via the LAMMPS MD package[27] using the Reactive Empirical Bond Order (REBO) force field[28–30] to model the interactions among Mo, W, S and Se atoms. We utilized the optimized parameters of Mo–S REBO for failure of the MoS_2 monolayer[31] and developed a reliable force field for other atoms with density functional theory (DFT) calculations[31,32]. We built a model composed of 4 nm MoS_2 and 6 nm WSe_2 in the y direction with 7 nm junction regions in the x direction along the interface on a simplified substrate. We applied a number of cyclic annealing processes, including relaxation of the structures from a high to a low temperature, and adding/deleting atoms on the basis of a Monte Carlo method. All processes are designed to accelerate the evolution of the 1D MoS_2 nanowire with natural bond forming and structural deforming (see more details in Supplementary Discussions 1–3). We utilized the VMD tool to visualize the simulations[33].

Code availability. We utilized the previously developed Mo–S REBO code for the LAMMPS MD package to handle four atoms: Mo, S, W, Se. The code is available in refs 27,28. Pseudocode for the extension and other simulation data are available from Markus J. Buehler (mbuehler@mit.edu) on request.

Data availability. All data generated and analysed during this study are available in the paper and its Supplementary Information. Extra data are available from the corresponding authors on request.

References

25. Hytch, M. *et al*. Quantitative measurement of displacement and strain fields from HREM micrographs. *Ultramicroscopy* **74,** 131–146 (1998).
26. Koch, C. T. *et al*. Useful plugins and scripts for digital micrograph. *Humboldt-Universität zu Berlin* https://www.physics.hu-berlin.de/en/sem/software/software_frwrtools (2016).
27. Plimpton, S. Fast parallel algorithms for short-range molecular-dynamics. *J. Comput. Phys.* **117,** 1–19 (1995).
28. Liang, T., Phillpot, S. R. & Sinnott, S. B. Parametrization of a reactive many-body potential for Mo–S systems. *Phys. Rev. B* **79,** 245110–245114 (2009).
29. Stewart, J. A. & Spearot, D. E. Atomistic simulations of nanoindentation on the basal plane of crystalline molybdenum disulfide (MoS_2). *Modelling Simul. Mater. Sci. Eng.* **21,** 045003–045015 (2013).
30. Brenner, D. W. *et al*. A second-generation reactive empirical bond order (REBO) potential energy expression for hydrocarbons. *J. Phys. Condens. Matter* **14,** 783–802 (2002).
31. Wang, S. *et al*. Atomically sharp crack tips in monolayer MoS_2 and their enhanced toughness by vacancy defects. *ACS Nano* **10,** 9831–9839 (2016).
32. Jung, G. S., Qin, Z. & Buehler, M. J. Molecular mechanics of polycrystalline graphene with enhanced fracture toughness. *Extreme Mech. Lett.* **2,** 52–59 (2015).
33. Humphrey, W., Dalke, A. & Schulten, K. VMD: visual molecular dynamics. *J. Mol. Graph.* **14,** 33–38 (1996).